AN EVALUATION OF FIRE PLUME PROPERTIES SIMULATED WITH THE FDS AND CLARK COUPLED WILDFIRE MODEL

by

Ruiyu Sun[1], Mary Ann Jenkins[2], Steven K. Krueger[1], William Mell[3], Joseph J. Charney[4]

[1]Department of Meteorology, University of Utah, Salt Lake City, UT USA

[2]Department of Earth & Space Science & Engineering, York University, Toronto, ON, Canada

[3]Building and Fire Research Laboratory, National Institute of Standards and Technology, Gaithersburg, MD USA

[4]United States Forest Service, North Central Research Station, East Lansing, MI USA

Corresponding author:
Ruiyu Sun
Department of Meteorology, University of Utah
Salt Lake City, UT, 84112, USA
rsun@met.utah.edu, (801)585-9487; (801)585-3681 (fax)

2006

ABSTRACT

Before using a fluid dynamical physically–based wildfire model to study wildfire validation is necessary, and model results need to be systematically and objectively analyzed and compared to real fires, which requires suitable data sets. Observational data from the Meteotron experiment are used to evaluate the fire plume properties simulated by two fluid dynamical numerical wildfire models, the Fire Dynamics Simulator or FDS, and the Clark coupled atmosphere–fire model. Comparisons based on classical plume theory between numerical model and experimental Meteotron results show that plume theory, because of its simplifying assumptions, is a fair but restricted rendition of important plume–averaged properties. The study indicates that the FDS, an explicit and computationally demanding model, produces good agreement with the Meteotron results even at a relatively coarse horizontal grid size of 4 m for the FDS, while the coupled atmosphere–fire model, a less explicit and less computationally demanding model, can produce good agreement, but that the agreement is sensitive to surface vertical–grid sizes and the method by which the energy released from the fire is put into the atmosphere.

1 Introduction

Wildland fire is a natural phenomenon involving complex chemical and physical processes. The range of length scales for each process is large, from the submillimeter scale (combustion process), to the kilometer scale (convection process), and then to the tens of kilometers or mesoscale (effects of terrain, shear environments, larger-scale weather systems, etc). Baum (2000) states that fires can be characterized by the nature of their interaction with the local environment, where the local environment is defined by the geometry and burning characteristics of the fuel bed, the properties of the ambient close–in atmosphere, and the local topography. In this study we focus on the interactions between the fire flame and the fuel (hereafter referred to as flame–fuel interaction), and between the fire flame and plume and the ambient atmosphere (hereafter referred to as flame+plume–atmosphere interaction). The flame–fuel interaction involves gas generation by solid fuel pyrolysis, the subsequent combustion of the fuel gases, and the resultant heat flux back to the solid fuel. The flame+plume–atmosphere interaction involves the response of the fire flame and plume to the ambient atmospheric conditions and the response of the atmosphere to the buoyant fire plume. This interaction can alter the orientation and geometry of the fire flame and plume, influencing the distribution and intensity of the net heat flux to the solid fuel and the burning of the fuel, and consequently changing the properties of local atmospheric conditions.

It is extremely difficult to study wildland fires by direct observation. Along with the cost and safety issues, controlled fire experiments require a great effort to achieve in a natural setting. For these reasons current computational fluid dynamical models are important tools for the study of wildfire, especially severe wildfire.

Because of the wide range of scales involved in a wildland fire, it is not possible to develop models that include all scales. Therefore, depending on the modeler's interests, each fire model concentrates on modeling wildfire behavior within a certain scale range. According to Mell et al. (2006), there are four basic types of models depending on whether the flame–fuel and/or flame+fuel-plume-atmosphere

interactions are involved: operational models that do not explicitly include the two interactions; models that mainly involve the flame+plume/atmosphere interaction; models that mainly involve the flame/fuel interaction; and models that include both interactions to a greater or lesser degree.

Operational models, such as FARSITE (Finney 1998) are built on semi–empirical formulas (Rothermel 1972). This type of model has low computational requirements and is aimed at providing field officers with real–time forecasts of the fire spread rate and intensity of wildland fires. Because operational models do not account directly for the flame–fuel and/or flame+fuel-plume-atmosphere interactions, the information these models provide is generally of limited accuracy. Despite the fact that they are prone to errors, the speed and simplicity of these models make them useful.

The Clark coupled atmosphere–fire model (Clark et al. 1996; hereafter referred to as the Clark coupled model) is an example of a wildfire model that emphasizes the interaction between the fire plume and the atmosphere. The model is designed to simulate wildland fires over scales where a typical computational grid size of 10s of meters is too coarse to resolve physical processes in the combustion zone. Evolving model winds from the lowest levels of the atmospheric fluid dynamical model are passed to an empirically or semi–empirically based operational fire–spread–rate formulation (e.g., Hirsch 1996, Rothermel 1972) which is used to advance the fireline (Clark et al. 2004). The Clark model is three–dimensional, nonhydrostatic, mesoscale numerical weather prediction model based on the Navier–Stokes momentum, thermodynamic, and conservation of mass equations. It includes multilevel grid nesting, and vertically–stretched and terrain–following coordinates that allow near-surface resolution in the vicinity of the fire and of flow in complex terrain. Moist processes are also represented with prognostic equations for water vapor and different water species (i.e., cloud condensate, rain water). The bulk warm rain parametermetization scheme of Kessler (1969) is used in the model. Readers are referred to Clark et al. (1996) for a complete model description and a list of references on the numerical framework on which the model equations are based.

Smagorinsky (1963) parameterization is used to control sub-grid-scale diffusion. Because the thermal degradation of the solid fuel is not modeled directly and combustion is parameterized, computational resources are devoted to resolving atmospheric physics.

Models that involve mainly the flame/fuel interaction are called "multiphase" models by most authors using this approach. This type of model was first presented by Larini et al. (1998) and subsequently used by others (Porterie et al. 2000; Morvan and Dupuy 2001; Morvan et al. 2002a,b; Zhou and Pereira 2000) to study flame spread through forest fuels. These models are the most physically complete models for flame/fuel interaction, but do not include the complete plume/atmosphere interaction.

Examples of a wildfire modeling approach similar to the multiphase models that involve both interactions are the Fire Dynamic Simulator (FDS) and FIRETEC. FIRETEC was designed at the Los Alamos National Laboratory (Linn 1997; Linn et al. 2002; Linn and Cunningham 2005) and built to analyze complex wildfire behavior that the current operational empirically–based wildfire models cannot represent. The FDS was designed at the National Institute of Standards and Technology (NIST) and was originally built to analyze industrial-scale fires. Mell et al. (2006) has extended the FDS to simulate outdoor fires in vegetative fuels. In these models the pyrolysis of fuels and gas phase combustion are implemented in a numerical solution of the Navier-Stokes equations, appropriate for low-speed, thermally-driven flow, with an emphasis on smoke and heat transport from fires. Computational resources are devoted to resolving fire combustion and the close–in fire/atmosphere flow over the fire. The WFDS is still defined by the historical FDS framework that is of interest in fire research: a single, relatively small, fire domain where the induced motions are nearly isobaric processes in an initially unstratified environment, with no terrain. The WFDS cannot represent the local weather within which wildfires burn. The future utility of the WFDS lies in the ability to depict fine-scale features such as the burning of isolated individual trees or the downwind transport of firebrands and smoke. Readers are referred to Mell et al. (2006) for a

complete description and overview of the WFDS modeling approach. Smagorinsky (1963) parameterization is used to control sub-grid-scale diffusion.

Pertinent to this study is that both the FDS and the Clark model are based on a so-called "anelastic" approximation, a term that needs to be clarified in the context of combustion–induced convection.

The "anelastic" approximation as applied to the Clark atmospheric model follows the approach of Ogura and Phillips (1962). In this set of model equations, the Ogura and Phillips anelastic approximation results when relative fluctuations in the thermodynamic variables are negligible (i.e., departure from their reference distribution is fractionally small), when the time scale of the motions is similar to that of gravity waves, and when the aspect ratio of the motions (i.e., the depth of the motions compared to the horizontal length scale) is not too large. If the time scale of the motions is similar to that of gravity waves, the time derivative of density can be safely neglected. The final equations (when linearized) contain only oscillations with frequencies less than the Brunt–Väisälä frequency, effectively filtering out higher frequency acoustic waves. If the depth of the motions is much less than the pressure scale height for an isothermal reference state and if the motions are strongly influenced by buoyancy forces, then the Ogura and Phillips anelastic set of equations can be further simplified to obtain the Boussinesq equations (Batchelor 1953).

The accuracy of the anelastic approximation by Ogura and Phillips (1962) depends on the magnitude of the excursions of the thermodynamic variables from the reference values. The approximation can be safely applied to the simulation of cumulus clouds and large boundary–layer eddies. In these situations, the departure of thermodynamic variables from the reference state is fractionally small (i.e., $\sim$ 1/300 for temperature). However there is no guarantee that the solutions obtained with the anelastic system will be consistent with the assumptions made in their derivation; as this study shows, it is possible to obtain solutions with the Ogura and Phillips anelastic system in which the departures of the thermodynamic variables from the reference state are not fractionally small. In a fire plume the relative

4

fluctuations in the thermodynamic variables are still fractional (i.e., $\sim 50/300$ for temperature), but larger than those in cumulus clouds or boundary–layer eddies.

As a consequence of the various approximations made, the Ogura and Phillips anelastic and Boussinesq set of equations have intrinsic errors on the order of a few percent for most atmospheric motions. The anelastic set of equations in the Clark model cannot model fire convection without losing some vorticity production. The constant pressure field that is the result of the Ogura and Phillips anelastic approximation has the effect of excluding the solenoidal term in the pressure gradient force. But as demonstrated by Clark et al. (1996), it is possible to restore, post analysis, model baroclinic vorticity. Clark et al. (1996) was also asked to consider the exclusion of baroclinic vorticity. Based on an investigation of a situation of strongly misaligned horizontal gradients of pressure and buoyancy, they were able to show that the forcing in fire-generated convective flow is dominated by the usual Ogura and Phillips anelastic baroclinic terms.

Classical plume theory (Morton et al 1956) is also used to investigate fire plume behavior. The plume properties that result from classical plume theory follow similarity theory — which is derived from the Boussinesq approximation. As the results of this study show, plume theory is reasonably successful in predicting global properties of the fire plume; the mean properties of the simulated buoyant plume are consistent with the self–similar vertical profiles of plume integrated buoyancy flux and vertical velocity described by Morton et al (1956). So, despite their limitations, the Ogura and Phillips anelastic and the Boussinesq set of equations have useful properties, and have been successfully employed in many studies of the evolution of convective thermals.

The "anelastic" approximation as applied to the FDS follows the approach of Rehm and Baum (1978). The equations of motion solved in the FDS are a low Mach-number approximation to the full Navier-Stokes equations. In obtaining these approximate equations, it is assumed only that the buoyancy-induced flow velocities are small compared to the speed of sound in the air. Therefore large temperature (and density) variations are permitted while sound waves, which result from the

elastic properties of the air, are eliminated or "filtered out." Such a gas may be described as "thermally expandable" because the density can change due to thermal fluctuations, but not change due to pressure changes. These equations are very different than those in the Ogura and Phillips "anelastic approximation," where sound waves are eliminated assuming approximately adiabatic conditions locally. Xin (2005) shows clearly that steep temperature gradients and the baroclinic torque are captured realistically by the FDS equations.

Though capable of accounting for almost all the variables that exist in wild-fire prediction, the computational fluid dynamical models — such as a coupled atmosphere–wildfire model and the WFDS — are not yet suitable for faster–than–real–time applications on today's computers. When run at the spatial scale of ~ 1 meter necessary to resolve FDS fire combustion and smoke, and the spacial scale fine enough to resolve the fine features of the coupled Clark model's fire/atmosphere interactions, the computational demands of the these models are presently too great to provide real–time forecasts of wildfire and fire spread in a landscape setting. Coen (2005) suggests that the Clark coupled model can be configured to run in faster than real time at coarse resolutions. But the coupled Clark model has yet to be validated for the faster–than–real–time applications. Models like FDS and Clark coupled model can be used to improve our comprehension of wildfire and the accuracy of operational wildfire models to forecast actual fire spread and behavior. Before applying these wildfire simulation models to these problems, model evaluation is necessary. We need to compare model results to real fires.

Proper model evaluation requires an appropriate set of field observations, taken under well–documented and controlled conditions, and carefully analyzed for fire behavior. However a major difficulty in developing realistic fire behavior and fire spread models is a lack of comprehensive field data for validation. Clements et al. (2005) discuss the few observational data sets that are available. The Meteotron Experiment (Benech 1976) is one of the first studies to specifically investigate the meteorology during a fire, and was designed to provide data for the theoretical study of a stationary, non-spreading, convective fire plume. In the Meteotron fire

experiment, Benech (1976) presented the results of measurements in and around convective plumes initiated in the atmosphere from the ground by an exceptionally powerful artificial heat source. The Benech (1976) study focused on idealized fire plume dynamics that do not necessarily completely represent wildfire/atmospheric interactions. Nonetheless, this is a valuable data set for model validation.

Our objective is model validation, and the purpose of this report therefore is to use the results from the Meteotron fire to examine how well the FDS and Clark model depict low–level structure/properties of this type of fire plume. A fire plume represents how the major portion of the energy from the fire's combustion process is put into the atmosphere and the resulting buoyancy distribution. Once we demonstrate here how accurately the FDS and the Clark coupled model simulate the properties and behavior of a stationary, non-spreading plume, we can begin to use WFDS, a physically–based multiphase fire model, to improve the fire parameterizations for spreading fires utilized by wildfire coupled models and the forecast accuracy of operational models like FARSITE.

The paper is organized as follows. The Meteotron experiment and data are outlined in the next section. Sections 3 and 4 describe the numerical experimental set-ups and the methods of analysis of the simulation results. Comparisons between the Meteotron and the simulated results are presented in section 5. A summary and discussion of the findings are given in section 6, and the paper is concluded in section 7.

2   The Meteotron Experiment

From 1971 to 1973 Benech (1976) conducted eleven atmospheric fire plume experiments during the Meteotron fire experiment. The heat source consisted of 97 oil burners arranged into a hexagonal area of about 4000 m^2 (radius 36 m). The experiments generally lasted five to ten minutes, and in most of the experiments the total theoretical thermal power was about 600 MW (0.15 MW m^{-2}). Measurements were taken using a radiosonde-radiowind system, kite balloons, photogrammetry from four observing stations, a ground network of temperature and wind velocity sensors, and an aircraft. The plume's geometrical parameters, including radius

(accuracy estimated at 10%) and vertical velocity at the visible boundary of the plume, delimited by thick black smoke, were determined by a photogrammetric method (Saporte 1966). Temperature and vertical velocity measurements were made directly in the plume with a radiosonde system using a kite balloon. Below 600 m, plume–averaged vertical velocity data were obtained with photogrammetry and the radio-sounding kite balloon, while at higher altitudes these data were obtained only with photogrammetry of the rising plume edge.

Benech (1976) claimed that the following plume properties remained practically identical below the first 600 m of elevation for all experimental fires:

- plume averaged radius at a given altitude;

- plume vertical velocities at a given altitude;

- vertical flux (m^3 s^{-1}) at a given altitude, deduced from the former data;

- and temperature difference (hereafter referred to as temperature excess) between the inside and the outside of the plume at a given altitude.

The following plume–averaged measurements at 10 m above ground level (AGL) were made:

- a temperature excess of 50 °C between the inside and the outside of the plume;

- a vertical component of the plume velocity of 3 m s^{-1}.

In the following sections, the FDS and Clark coupled model simulations are compared to the Meteotron mean plume radius, vertical velocity, mass flux, and temperature excess (temperature difference between the plume–averaged temperature and environment–averaged temperature) taken, respectively, from Figures 5, 6, 7, and 8 in Benech (1976), and the mean plume buoyancy flux constructed with these data.

8

3   Numerical Experimental Set-up

A single FDS simulation and two Clark coupled model simulations were completed, and results from the simulations are compared to each other and to the observational data from the Meteotron fire experiment.

The version of FDS used in this study is described by McGrattan and Forney (2004) and Mell et al. (2006). The FDS domain was 400 m (x) $\times$ 400 m (y) $\times$ 600 m (z) and covered by a grid mesh of 100 (x) $\times$ 100 (y) $\times$ 100 (z). The FDS is designed to run with a grid size small enough to resolve the large flames in a fire. For the Meteotron plume, the burners covered an area of $\sim$ 75 m across. The 4 m grid size gives the more than 10 grid points that are needed to resolve the flame–scale features. The vertical grid was stretched and vertical grid size was about 3 m near ground level. The model atmosphere was isothermal, with an ambient temperature of 30.85°C. As discussed in the Introduction, the FDS was originally built to analyze industrial-scale fires, where the model fire domain is small, and an initially isothermal environment is the default. This study focuses on the lower portion of the fire plume, below the first 300 m of elevation, where the temperature excesses in the plume are significantly ($\sim$ 50°C) large compared to the environment. The impact of the default isothermal, as opposed to a neutral, lapse rate on fire–induced convection over such a shallow surface layer is therefore relatively small. A uniform wind of 3 m s^{-1} and constant with height blew into the domain from the west (in the positive x direction). To match the size and total heat release rate of the Meteotron fires (4000 m^2; 600 MW), a square fire of 63.25 m $\times$ 63.25 m was set. The heat release rate per unit area was used to specify the heat release rate of 150 kW m^{-2} and the simulation lasted 700 seconds.

The version of the Clark coupled model used in this study is described by Clark et al. (1996) and Clark et al. (2004). The two simulations by the Clark coupled model, denoted as *Clarka* and *Clarkb*, were initiated in an environment of neutral stability with a surface temperature of 30.85°C and pressure of 100 kPa. The observed plume properties are averaged from 11 Meteotron experiments, and below 600 m above ground level, the averaged atmospheric lapse rate from these

9

experiments was roughly neutral. The background wind was uniform at 3 m s^{-1} from the west and constant with height. The x and y horizontal grid interval was 25 m. The vertical grid was stretched and vertical grid size was about 10 m near the ground. Two domains were used in the simulations, an inner domain 1.2 km $\times$ 1.2 km in area nested in an outer domain 6.45 km $\times$ 6.45 km in area. Simulations used 86 vertical levels in the inner domain, and the inner domain extended to an altitude of 6.2 km. A sensible heat flux of 160 kW m^{-2} was assigned to six surface–level grids in the inner domain so that the total surface heat release rate came to 600 MW as in the Meteotron experiment. The six surface grids made the total burning area in the Clark coupled model 3750 m^2, which given the 25 m horizontal grid size was as close as possible to the total burning area of Meteotron fire (4000 m^2). Fire combustion was represented by the surface sensible heat flux, and an assumption was made that roughly 30% of the total heat released by the model fires was lost by radiation to the surroundings (Koseki and Mulholland 1991, about the same amount of total energy is lost in the FDS simulation). Only the heat remaining after the loss of radiation is exchanged directly with the atmosphere. The Clark coupled model is designed to run with a grid size that resolves the fire convection, while the fire spread model represents the averaged effects of the sub–grid flame–scale features (i.e., combustion, radiation, ignition, and turbulence). Simulations lasted an hour.

Clark et al. (1996) used a simple extinction approach to treat the fire-atmosphere heat exchange to avoid excessive local heating of the atmosphere when the entire sensible heat released from the fire was deposited in a column above the fire. In this early work it was not possible to test whether this simple extinction–depth approach was realistic or even necessary. Therefore, in this study, the sensible heat flux of the fire was put into the Clark coupled model atmosphere in two different ways. In simulation *Clarka*, the surface sensible heat was vertically distributed in the atmosphere over an *e*-folding distance or extinction depth of 50 m. In simulation *Clarkb*, all the surface sensible heat was put into the first vertical layer in the inner domain.

4 Method of Analysis

Time–mean plume–averaged vertical velocity, temperature excess, effective plume radius, plume mass flux, and buoyancy flux were calculated for each simulation. Time mean values were the averages of instantaneous plume properties after the plumes were fully developed (at approximately 200 seconds into the simulations). The Clark plumes were considered fully developed when the buoyancy field reached a quasi–steady state. The FDS plume was considered fully developed when the smoke plume reached a quasi–steady state. Accurate calculations of plume–averaged properties are dependent on an accurate determination of the edge of the plume. Benech (1976) used "thick black smoke" and a photogrammetric method (Saporte 1966), with an estimated accuracy of 10%, for plume edge determination in the Meteotron experiment. Using the plume soot density provided by the FDS simulation, photos of smoke, as in Figure 1, were generated based on a version of Beer's law used by Smokeview, the software visualization tool for FDS (Forney and McGrattan 2004). These photos were overlaid on a cross-section of soot density along the centerline of the fire domain (y=0). A soot density of 0.5 mg m^{-3} was selected to delineate the plume edge and effective radius. Locations with soot density greater than 0.5 mg m^{-3} were considered to be inside in the plume. This choice of plume edge criterion (referred to as soot plume hereafter) was supported by radial profiles of soot density at different height levels. Figure 2 shows how, at 600 s into the FDS simulation, soot density varies along the center line of the domain in the x direction and along the line through the point with the maximum soot density in the y direction. At lower levels (below 300 m), the area with soot density greater than 0.5 mg m^{-3} covered almost all the plume. For this reason, the results presented in this study focus on the lower portion of the fire plume.

The soot plume can not be used to determine plume properties in the Clark coupled model simulations. The Clark (1996) coupled model does not simulate smoke and soot (the version of the model described by Clark et al. 2003 does simulate smoke, but was not available for this study), and therefore no direct comparison can be made between fire plumes in the Clark coupled model simulations and the

Meteotron experiment. However comparisons can be made between the FDS and Clark coupled model plumes when each model's plume–averaged properties depends on a consistent determination of the plume's edge. It was assumed that the radial profile of vertical velocity w in the plume has a normal distribution (McCaffrey 1983), and the portion of each plume with

$$w > \frac{w_{\mathrm{max}}}{\exp(c)},$$ (1)

where w_{max} is the plume's maximum vertical velocity, was selected for plume property calculations and comparisons between the simulations. Hereafter this method is referred to as the W plume. Based on Yih (1951), the constant c is given the value 1.38 in Equation 1.

Computational resources were limited for this study. Only earlier serial versions of the FDS and Clark coupled model were workable for this study. Simulations were completed on a single processor on the University of Utah's Center for High Performance Computing (CHPC) Icebox cluster. The Cluster had 303 nodes and 388 processors. The CPU speeds on the nodes ranged from 350 Mhz to 1533 Mhz (most node speeds about 1000 Mhz). Depending on processor speeds, run times were about 10 hours for the FDS and 70 hours for the Clark coupled model simulations. Since most nodes had a memory capacity below 1024 MB, the domain size for each simulation was restricted.

As a result the horizontal domain sizes were not large enough to contain model simulations, and the fire plumes went out of the lateral boundary on the downwind side of the domain before they reached domain top. The plume started to go out of bounds at approximately 300 m AGL in the FDS simulation (Figure 1) and at approximately 340 m AGL in the Clark coupled model simulations (not shown). Above these heights, plume–averaged properties were calculated based on the portions of the plumes inside of the domains. Again, consequently, the results presented in this study focus on the lower portion of the fire plume, below the first 300 m of elevation.

5 Simulation results

5.1 Comparing Meteotron and FDS plume properties

Figure 3 shows vertical profiles of the Meteotron, and soot–plume and W–plume FDS plume–averaged temperature excess, vertical velocity, effective radius, and mass flux. Each temperature excess profile is similar in shape, decreasing quickly with height near the surface. Plume–averaged vertical velocity $\overline{w}$ profiles are also similar in shape but different in magnitude. At lower levels the W–plume tends to have a bigger plume–averaged temperature excess and vertical velocity, and smaller plume–averaged radius than either the FDS soot–plume or Meteotron plume. The differences between these profiles are due primarily to the soot plume including areas of negative and small values of w, while the W plume does not. Although not apparent from these profiles, but easily deduced from Figure 1, the FDS results show large fluctuations in $\overline{w}$ due to turbulent motion (shedding of large eddies by the convection); strong updrafts coexisted with weak updrafts, sometimes even downdrafts in the plume, which contributed to the overall smaller soot–plume averaged FDS $\overline{w}$. Effective radii in the simulated plumes were determined by calculating plume area in the horizontal and assuming that the plume edge is a perfect circle. The Meteotron effective R and $\overline{w}$ were taken from Figures 5 and 6 in Benech (1976). Figure 3 shows that the W and soot FDS plume radii are slightly different near the ground but similar aloft ($\sim$ above 200 m). At levels above 100 m, the effective plume radii determined by the FDS soot and W plumes are considerably smaller than the plume radius taken from Figure 5 in Benech (1976).

Figure 3 also shows the vertical profiles of plume mass flux calculated using

$$F_M = \overline{w}\pi R^2, \tag{2}$$

where $\mathbf{F}_M$ is the plume mass flux according to classical idealized plume theory, and $\overline{w}$ and R the plume–averaged vertical velocity and effective radius, respectively. The differences between Meteotron and the FDS plume mass flux are due mainly

13

to the dependence of mass flux on R^2. Figure 3d shows that there is agreement only near the surface (~ 100 m) where the W and soot FDS plume radii are almost identical to the Meteotron R. At higher levels the total plume mass flux in FDS is only about half as large as the Meteotron F_M.

The reason for attributing the discrepancies between the vertical profiles of the Meteotron and the FDS plume mass flux to R^2 is seen in Figure 4 which shows x-y cross-sections of the FDS soot–plume at 103 m and 201 m AGL near the end of the simulation (680 s, arbitrarily picked). The outermost soot contour is 0.5 mg m^{-3}, corresponding to the edge of the plume. As in Figure 1, the shape of the plume is highly irregular, especially at the upper 201 m level. Figure 4 shows that if the FDS plume is viewed from a different angle, the difference in radius can be as large as 1/3 the effective radius. Figure 5a shows how different plume–averaged effective radii are possible. Figure 5b shows that when the average value of the x direction and y direction bounded radii shown in Figure 5a and the averaged vertical velocity in the soot plume are used in the mass flux calculation, the FDS mass flux is closer to the Meteotron result than calculations based on the plume edge as a perfect circle. Note that the plume radius determined by a photogrammetric method in the Meteotron experiment is, for the same reasons, only an estimate of the actual plume radius. Furthermore, because the Meteotron F_M was constructed using data from plots of vertical profiles of $\overline{w}$ and R in Benech (1976), there is additional uncertainty in the calculation of the Meteotron mean plume buoyancy flux. Good agreement between Meteotron and simulated FDS plume properties therefore depends on the method and accuracy of the data analysis.

5.2   Comparing FDS and Clark coupled model plume properties

The FDS model is being used here to determine what the Clark coupled model should produce, and the way to make congruous comparisons between the simulated plume properties from the two models is to average the FDS results to the scale for which the Clark coupled model is predicting. Data in the FDS simulation were averaged horizontally and vertically to 24 m and near-ground 10 m grid sizes — as

close as possible to the 25 m horizontal and 10 m vertical grid sizes in the Clark coupled model simulations — before calculating the plume properties based on the W plume. Horizontally averaged FDS grid values will hereafter be refereed to as a grid–area average, and horizontally and vertically averaged FDS grid values as a grid–volume average. Unless stated otherwise, all following comparisons between FDS and *Clarka* and *Clarkb* are based on grid–volume averaged FDS results.

Figure 6 shows the differences in the plume properties between before and after FDS averaging. Differences are most significant in the plume–averaged temperature excess and vertical velocity at levels below 300 m, where magnitudes were most reduced by this averaging. A comparison between Figures 6 and 3 shows that averaging of FDS data produced, incidentally, upper-level plume properties of larger magnitude than the Meteotron results.

Figure 7 shows W-plume vertical profiles of the plume–averaged temperature excess, $\overline{w}$, R, and plume mass flux F_M for the FDS and the Clark coupled model simulations. Compared to FDS, the coarser horizontal and vertical resolutions in the Clark simulations resulted in substantially smaller plume temperature excesses and vertical velocities, especially below the first ~ 50 m of elevation, and especially for *Clarka*. In *Clarkb* sensible heat from the fire was put into the lowest vertical layer in the model, and convection resolved by the Clark model took over to distribute and transport the energy. In *Clarka*, the same amount of the energy was distributed vertically, over more than one layer, resulting in a smaller and unrealistic temperature excess near the ground. Above 50 m AGL the plume–averaged temperature excesses in *Clarka* and *Clarkb* become essentially equal.

Figure 7b shows the vertical profiles of $\overline{w}$. Although all three profiles are similar in shape, both Clark coupled simulations show significantly smaller $\overline{w}$ values compared to $\overline{w}$ in the FDS simulation. Since $\overline{w}$ in a convectively–driven plume is dominated by vertically integrated buoyancy, which is determined by plume temperature excesses, these differences in profiles are due to the fact that, in the lower portion of the plume, there was immediately more buoyancy in the FDS plume grid-scale volume averages compared to *Clarkb*, and then compared again to

15

Clarka.

Figure 7c shows that the W–plume Rs in *Clarka* and *Clarkb* are significantly larger than the corresponding Rs in the FDS simulation. Consequently the plume–averaged mass fluxes in *Clarka* and *Clarkb*, seen in Figure 7d, are also significantly larger than those in the FDS simulation, and coincidentally more comparable in magnitude and behavior to the Meteotron soot–plume radius and mass flux shown in Figure 3.

5.3   Comparing plume properties at 10 m AGL

Plume–averaged temperature excess and vertical velocities at 10 m AGL for the simulations and the Meteotron experiment are summarized in Table 1. Compared to the Meteotron temperature excess and vertical velocity, the FDS simulation produced a smaller soot–plume averaged temperature excess of 23^oC, and a smaller $\overline{w}$ of 1.4 ms^{-1}. It appears that FDS plume averages are sensitive to the soot threshold used in the soot plume; e.g., when 7.5 mg m^{-3} was used, instead of 0.5 mg m^{-3}, $\overline{w}$ was closer to 3.0 m s^{-1}. The Meteotron $\overline{w}$ was based on an average of only several measurements inside the plume and is possibly an overestimate. When the W plume is used, both the FDS plume–averaged temperature and vertical velocity at 10 m AGL are much closer to the Meteotron results. In the Clark coupled model simulations, the W–plume averaged temperature excess and $\overline{w}$ at 10 m AGL are smaller than those in FDS using the same W plume after averaging. The plume–averaged temperature is very much smaller in *Clarka*, where the sensible heat was distributed in the atmosphere over the extinction depth of 50 m, than in *Clarkb*, where all surface sensible heat was put into the first 10 m vertical layer. The mean grid-scale heating that results from an average of the atmospheric temperature ($\sim$ 300 K) and the combusting fuel temperature ($\sim$ 800 to 1200 K) times the mean vertical velocity is contingent on the total surface heat release rate which limits the heat flux.

5.4   Comparing Meteotron and simulated buoyancy fluxes

The buoyancy flux for the FDS simulation and the Clark coupled model simulations were analyzed, first within the confines of classical plume theory, and then using a more fundamental approach based on conservation of energy and mass, where by combining the conservation of mass and energy model equations, an expression for conservation of buoyancy flux is produced (Appendix).

According to classical plume theory, convective buoyancy flux F_B is determined by

$$F_B = \overline{w}\,\overline{B}\,\pi R^2 \qquad (3)$$

where $\overline{w}$, $\overline{B}$, and R are, respectively, the plume–averaged vertical velocity, buoyancy, and effective radius. Using this equation for F_B, Figure 8 shows the vertical profiles of the convective buoyancy flux for the Meteotron experiment and for the W– plume fire simulations. With the exception of *Clarkb* at $\sim$ 20 to 30 m elevation, the Meteotron F_B is considerably larger than the convective buoyancy flux from the simulations. Again, the Meteotron results reflect the entire plume radius as defined by visible smoke boundaries of the observed plumes, while the vertical profiles of convective buoyancy flux for the simulated plumes reflect the partial, W–plume as defined by the effective radius in classical plume theory. Also the Meteotron buoyancy flux profile for F_B was deduced from plots of mean plume radius, vertical velocity, and temperature excess in Benech (1976), and not based on original observations. The Meteotron $\overline{B}$ assembled from these data is considered especially vulnerable to error at levels below 50 m, primarily due to the difficulty establishing an accurate temperature excess reading from Benech (1976). The spike in buoyancy flux near the ground in *Clarkb* is a result of depositing the entire sensible heat released from the fire into the first model layer above the fire. The FDS convective buoyancy flux profile lies between the *Clarka* and *Clarkb* profiles.

More generally, convective buoyancy flux F_B can also be determined by

$$F_{B(grid)} = \int_{plume} <w><B>\, dA, \qquad (4)$$

a straightforward spatial averaging of the product of grid values of vertical velocity $<w>$ and buoyancy $<B>$, where dA is the horizontal area of each grid, and the total area remains confined by R as in Equation 3. Figure 9 shows the vertical profiles of the convective buoyancy flux of the W–plume fire simulations, calculated using Equation 4, and of the Meteotron experiment F_B. Compared to the model F_B values based on Equation 3, Equation 4 produced larger convective buoyancy fluxes, particularly in the first 50 meters AGL, which are overall more in line with the Meteotron F_B. The FDS convective buoyancy flux profile now lies closer to the *Clarkb* profiles for the first 300 m

The vertical profiles of the model domain area–averaged $F_{B(grid)}$ for each simulated plume (not shown) reveal very little difference between $F_{B(grid)}$ profiles based on either soot or W plume–edge criterion or domain area–averaged values, indicating that the (especially soot) plume–edge criteria were good plume–determination criteria.

Conservation of buoyancy in the FDS simulation is determined by

$$\int_V \frac{\partial B}{\partial t}\, dV + \int_{\partial V} B\, \vec{\mathbf{v}}_H \cdot \widehat{\mathbf{n}}\, dS + \int_{bottom}^{top} B\, w\, dS = -\int_{\partial V} \vec{\mathbf{F}} \cdot \widehat{\mathbf{n}}\, dS, \qquad (5)$$

where all variables in Equation 5 are defined in the Appendix. The terms on the left-hand side of Equation 5 are, respectively, buoyancy storage, buoyancy change due to the horizontal advection, and buoyancy change due to the convection in the layer. The term on the right-hand side is the buoyancy change due to sub–grid scale (SGS) motion, radiation, and combustion. Given the boundary conditions, where $\vec{\mathbf{F}}=0$ at the top of the simulation domain, Equation 5 is used to calculate the FDS buoyancy flux $\vec{\mathbf{F}}$ at different height levels, where the total vertical buoyancy flux is the sum of the convective buoyancy flux and the vertical buoyancy flux due to the SGS motion, radiation and combustion.

Conservation of buoyancy in the coupled Clark simulations is determined by

$$\int_V \frac{\partial B}{\partial t}\,dV + \int_{\partial V} B\,\vec{\mathbf{v}}_H \cdot \widehat{\mathbf{n}}\,dS + \int_{bottom}^{top} B\,w\,dS =$$
$$\frac{g}{C_p\,\overline{\rho}\,\theta_e} \int_V \nabla \cdot (C_p\,\overline{\rho}\,K_H\,\nabla\theta)\,dV - \frac{g}{C_p\,\overline{\rho}\,\theta_e} \int_{\partial V} C_p\,\overline{\rho}\,\theta_e\,\vec{\mathbf{v}} \cdot \widehat{\mathbf{n}}\,dS, \qquad (6)$$

where all variables in Equation 6 are defined in the Appendix. The difference between Equations 5 and 6 lies in the terms on the right-hand side of these equations. In Equation 6 these terms represent, respectively, the buoyancy change due to SGS heat flux and to the environmental heat flux. Because the Clark simulations were initiated in an environment of neutral stability, the environmental heat flux term in Equation 6 is zero. The total buoyancy change in the layer due to the resolved and unresolved vertical motion in the Clark coupled model simulations is therefore the sum of the vertical convection term, and the SGS heat flux term.

FDS profiles of the total vertical buoyancy flux, buoyancy flux by convection, and vertical buoyancy flux by SGS motion, radiation and combustion, based on Equation 5, before and after grid–area averaging, are given, respectively, in Figures 10a and 10b. Total vertical buoyancy flux is essentially constant below 300 m, the height the FDS plume began to move out of the lateral domain boundary. Below $\sim$ 30 m, the convective buoyancy flux increases rapidly with height, while the SGS flux decreases rapidly with height. Above 30 m, convective buoyancy flux dominates to contribute to the total buoyancy flux, while SGS flux declines, quickly in Figure 10a and more gradually in Figure 10b, to near–zero values. Again, although not apparent from the profiles in Figure 10a, there are large fluctuations in FDS convective flux values due to turbulent motion. Consequently, Figures 10a and 10b show that the grid-scale convective buoyancy flux is made smaller and positive, while the sub-grid scale convective flux is made larger and all positive, by grid–area averaging.

Profiles of the total vertical buoyancy flux, buoyancy flux by convection, and the SGS heat flux based on Equation 6 for *Clarkb* and *Clarka* are given, respectively, in Figures 10c and 10d. The *Clarka* results (Figure 10d) are more similar to the grid–area averaged FDS results (Figure 10b), while the *Clarkb* results (Figure 10c)

19

are more similar to the before grid–area averaged FDS results (Figure 10a), in both behavior and magnitude. Note that there is little discernible difference between any of the profiles of the total vertical buoyancy flux in Figure 10.

The differences between Figures 10a and 10d are that *Clarkb* shows an even more abrupt increase with height in the convective buoyancy flux, and an even more abrupt decrease with height in the SGS flux in the first 30 m AGL. Above 30 m, the change with height stops and the convective buoyancy flux dominates to contribute almost entirely to the total buoyancy flux, while SGS flux falls to small near-zero (but all positive) values.

The differences between Figure 10b and 10c are that *Clarka* shows an even more gradual near-surface increase with height in the convective buoyancy flux, and an even more gradual decrease with height in the SGS flux, which eventually stop at ~ 100 m AGL not ~ 30 m AGL, compared to the *Clarkb* and the before grid–area averaged FDS profiles. Above 100 m, the *Clarka* SGS flux profile remains positive and non–negligible, making a relatively substantial contribution of the total buoyancy flux, while the contribution by the convective buoyancy flux is diminished compared to the FDS profile in Figure 10b.

Grid–scale buoyancy is a volume average of buoyancy of the combusting fluid and the atmosphere, while the fire–induced buoyancy is confined to the region containing combusting gases. Since FDS radiative and SGS scale energy transport calculations are more explicit and more realistically confined to regions containing combusting gases, it is assumed that the FDS profiles in Figure 10 correspond most closely to reality. By comparison, it appears that in *Clarkb* buoyancy was put into too shallow a surface layer by the SGS heat flux, and that in *Clarka* buoyancy was put into too deep a surface layer by the SGS heat flux.

6   Discussion

The FDS and the Clark coupled atmosphere–fire model, representing two types of fluid dynamical wildfire models, are used to simulate stationary, non-spreading fires in the Meteotron fire experiment and evaluated based on comparisons between Meteotron and simulated model fire plume properties. Along with fundamental

differences between the two numerical models, agreement between Meteotron and simulated plume properties depended on both experiment and numerical model design, and the method of analysis of Meteotron and numerical model data. The numerical set-ups only approximated the environmental conditions during the Benech study. For example, in the FDS simulation the atmosphere was isothermal and in the Clark coupled model simulations the atmosphere was neutrally stable, while background winds in every simulation were constant in speed, direction, and height. An exact match to the Meteotron total burning area was not possible. Much of the analysis of the data and comparison of results depended on classical plume theory. Agreement between plume–averaged properties is constricted by a plume theory rendition, given its simplifying assumptions and idealized boundary conditions. Plume theory depends on plume–averaged properties based on accurate estimations of plume edge and an effective plume radius. Benech (1976) rated the accuracy of plume properties to be $\pm 10\%$. This study shows that the different methods for determining effective plume radius affect the analysis. Depending on the method of analysis, agreement exists between the Meteotron and FDS soot–plume properties, and between the FDS and Clark coupled model W–plume properties.

Comparisons of the FDS plume–averaged properties to the Meteotron experiment indicate that, depending on the plume edge (soot or W) and the subsequent determination of effective radii and use of classical plume theory, the plume–averaged temperature excess and vertical velocity showed good agreement with the Meteotron experiment, while the plume–averaged effective radius and mass flux showed good agreement depending on the method of analysis. Comparisons of *Clarka* and *Clarkb* to the FDS W–plume averaged properties results indicate that the plume radius and mass flux in *Clarka* and *Clarkb* were similar, larger than FDS results. Near-surface temperature excess and vertical velocity were smaller in *Clarka* than in *Clarkb*, and both were smaller again than FDS results.

The Meteotron results and the FDS simulation demonstrate that the FDS can provide realistic plume–averaged properties. The comparisons between the FDS simulation and the Clark model simulations show that the coarser resolution of

21

the coupled Clark model does reduce the accuracy of plume properties. Better agreement, especially in the first 10 to 30 m of elevation, between the Clark model and the Meteotron and FDS plume–averaged temperature excess and vertical velocity results was obtained when all the surface sensible heat was put into the first vertical layer (10 m elevation) of the coupled Clark model.

Using Meteotron as a benchmark, the Meteotron, FDS, *Clarka*, and *Clarkb* buoyancy flux profiles indicate the following. Depending on the method of determination, the FDS and *Clarka* buoyancy flux showed similar overall behavior and magnitude, and fair to good agreement with the Meteotron experiment at elevations greater than 50 m AGL. As a result of depositing the entire sensible heat from the fire into the first 10 m AGL of the model atmosphere, *Clarkb* showed an abrupt spike in buoyancy flux near ground level, below the 50 m AGL, in partial agreement with the Meteotron experiment (shown) and before averaging FDS values (not shown).

Using FDS as a benchmark, the FDS, *Clarka*, and *Clarkb* conservation of buoyancy flux analysis indicates the following. The buoyancy flux by SGS motion and heating were more active close to the flaming zone of a fire, and directly influenced the vertical transport of energy only at near-surface elevations (which ranged from $\sim$ 30 to 100 m depending of the method of determination). At near-surface elevations, the convective buoyancy flux increased (very rapidly depending on the method of determination) with height, while the SGS flux decreased (very rapidly depending on the method of determination) with height to near–zero. At above near–surface elevations, the convective buoyancy flux made up almost the entire total vertical buoyancy flux, which was essentially constant with height.

Based on comparisons of the *Clarka* and *Clarkb* to the FDS and the Meteotron results, there is no clear, unambiguous choice of whether it is better to deposit the sensible heat released from the fire over a relatively large extinction depth of 50 m, as in *Clarka*, or over a first 10 m vertical layer as in *Clarkb*. The first method underestimates important near-surface properties just above the fire, such as temperature excess and vertical plume velocity, while the second method produces a too abrupt and discrete spike in convective buoyancy flux just above

22

the surface model grid layer.

It seems likely then that a coupled model simulation would achieve more reasonable plume–averaged properties if a realistic extinction depth is adopted. Although the extinction depth depends on a number of parameters, such as fire intensity, flame height, burning fuel, the environment of the fire, etc., it is possible to estimate roughly what the extinction depth should be with

$$I/I_0 = e^{-KL}, \tag{7}$$

a form of Beer's law. Here I_0 and I are the radiation intensities at a wavelength before and after the extinction occurs, K is the extinction coefficient, and L is an attenuation length. Assuming that soot is the most important combustion product controlling the thermal radiation from the fire flame and hot smoke, then the extinction coefficient is $K = K_m \rho_s$, where K_m and ρ_s are the mass specific extinction coefficient and soot density. For flaming combustion of wood, K_m is 7600 m^2 kg^{-1} (McGrattan and Forney 2004). The averaged soot density below 100 m AGL was approximately 5 mg m^{-3} in the FDS simulation. Based on these assumptions, the approximated e–folding extinction depth is $\sim$ 25 m from the flame height, less than the 50 m extinction depth used in part of this study. However, it should be noted that there is no universal e–folding extinction depth. The e–folding extinction depth varies depending on the specific fire situation, and will be bigger in a tree crown fire than in a grass fire. Measurements during FROSTFIRE crown fires suggested the e–folding extinction depth of 50 m (Coen et al. 2004).

7 Conclusions

The FDS and Clark coupled atmosphere–wildfire model are evaluated by comparing the predictions of fire plume behavior to the Meteotron (Benech 1976) observations. The Meteotron experiment was designed to provide data for the theoretical study of a stationary, non-spreading, convective fire plume generated by an artificial heat source which resulted in a straightforward specification of heat release rate. As a consequence this study has only a limited number of plume properties to examine, and serves as a relatively simple and appropriate first step to assessing these models.

The study has demonstrated that comparisons between the FDS, a physically–based multiphase fire model, and Meteotron plume observations show that the FDS is capable of rendering realistic plume–averaged temperature and vertical velocity profiles in a stationary, non-spreading, almost entirely buoyancy–driven, convective fire plume. Comparisons between the FDS and Meteotron plume observations show that good agreement between the vertical profiles of the Meteotron and the FDS plume radius and mass flux depends on the method and accuracy of the plume radius analysis. The study has also demonstrated that the Clark coupled model, designed to simulate wildland convection associated with large fire plumes and their environment, is likewise capable of rendering comparatively realistic plume–averaged properties, even when fire combustion is represented simply by a surface sensible heat flux, provided that the energy released from the fire is distributed vertically into a layer whose ideal depth is greater than flame height and close to the extinction depth. Accurate sensible heating amounts and rates, and a stretched grid allowing for finer near-surface grid resolution, based on an energy extinction depth appropriate to the fire, are recommended to achieve realistic plume properties in a coupled model.

According to classical plume theory (Morton et al. 1956), one of the external parameters determining plume–averaged properties such as buoyancy and vertical plume velocity in a convective plume is the buoyancy flux at the source. If vertical velocity is known, then vertical mass flux is known, and vice versa. If vertical mass flux is known, then inflow velocity can be determined. Mass flux, vertical velocity, and inflow velocity are all related to plume height through atmospheric stability. Inflow velocity at the surface is connected to fire spread rate, which is connected to fire combustion and sensible heat flux at the ground. These concepts based on classical plume theory contribute to our understanding of fire plume behavior.

Benech (1976) estimated that the water vapor mixing ratio by combustion increased by 1.37 g kg^{-1} in the Meteotron fire experiment. The resulting increase in the plume's buoyancy was less than that due to a 1 K temperature excess. A possibly important aspect to model plume dynamics that could not be evaluated

from the Meteotron fire is the role of latent heating (due to condensation of water vapor) and the implication for buoyancy. In a pilot study to measure water vapor, heat, and carbon dioxide fluxes within a single prescribed Texas prairie fire, Clements et al (2005) indicate that a grass fire can modify the dynamic environment by adding significant amounts of water vapor as well as heat into the lower atmosphere, while Potter (2005) has attempted to explain the latent heat implications for buoyancy. Coupled wildfire–atmospheric models, such as the Clark coupled model, are capable of examining these aspects of fire in more detail. This is future work.

The next step is to extend the model validation effort to a larger set of experiments (e.g., non–stationary, not almost–exclusively buoyancy driven, spreading fires) and to a wider range of fuel types and fuel parameters (e.g., moisture, surface–to–volume ratio, packing ratio) in order to assess both WFDS and coupled atmosphere–wildfire model capabilities.

Once evaluated, we plan to use these numerical dynamical wildfire predictions models to develop more realistic parameterizations of fire spread rate and fire intensity for coupled wildfire models. Numerical models that couple wildfire to the atmosphere recognize that combustion occurs at subgrid scales and consequently must be parameterized. A coupled atmosphere–wildfire model's ability to accurately predict local, possibly erratic, wind and the interaction of fire and wind makes it a valuable tool for studying severe fire behavior or large pyrocumulus development. The best use of these model types is to improve our comprehension of wildfire-atmosphere interactions and the ability of operational models to forecast actual wildfire spread and behavior under a wide range of conditions.

REFERENCES

Batchelor, G., 1953: The conditions for dynamical similarity of motions of a frictionless perfect-gas atmosphere. *Quart. J. R. Meteor. Soc.*, **79**, 224–235.

Baum, H. R., 2000: Modeling and scaling laws for large fires. In *Proceedings of ISSM-III Third International Symposium on Scale Modeling*, Nagoya, Japan, 1–13.

Benech, B., 1976: Experimental study of an artificial convective plume initiated from the ground. *J. Appl. Meteor.*, **15**, 127–137.

Clark, T., J. Coen, and D. Latham, 2004: Description of a coupled atmosphere-fire model. *International J. of Wildland Fire*, **13**, 49–63.

Clark, T., M. Griffiths, M. J. Reeder, and D. Latham, 2003: Numerical simulations of grassland fires in the northern territory, australia: A new subgrid–scale fire parameterization. *J. Geophys. Res.*, **108(D18)**, 4589, doi:10.1029/2002JD003340.

Clark, T., M. A. Jenkins, J. Coen, and D. Packham, 1996: A coupled atmosphere-fire model: role of the convective froude number and dynamic fingering at the fireline. *International J. of Wildland Fire*, **6**, 177–190.

Clements C. B., B. E. P., and S. Zhong, 2005: In-situ measurements of water vapor, heat, and co2 fluxes within a prescribed prairie fire. *International J. of Wildland Fire*, **Accepted**.

Coen, J., 2005: Simulation of the big elk fire using coupled atmosphere–fire modeling. *International J. of Wildland Fire*, **14**, 49–59.

Coen, J., S. Mahalingam, and J. Daily, 2004: Infrared imagery of crown-fire dynamics during frostfire. *J. Appl. Meteor.*, **43**, 1241–1259.

Finney, M. A., 1998: FARSITE: Fire Area Simualtor-Model, Development and Evaluation. Technical Report RMRS-RP-4, USDA Forest Service, Rocky Mountain Research Station Paper.

Forney, G., and K. McGrattan, 2004: User's guide for smokeview version 4; a tool for visualizating fire dynamics simulation data. Technical report, NIST. NIST Special Publication 1017.

Hirsch, K. H., 1996: Canadian forest fire behavior prediction (fbp) system: User's guide, special report 7. Technical report, Canadian Forest Service, Northwest Region, Northern Forestry Center.

Kessler, E., 1969: On the distribution and continuity of water substance in atmospheric circulations. In *Meteor. Monogr.*, number 32, Amer. Meteor. Soc., p84.

Koseki, H., and G. W. Mulholland, 1991: The effect of fire diameter on the burning of crude oil pool fires. *Fire Technology*, **27**, 54–65.

Larini M., F. Firoud, B. P., and J. C. Loraud, 1998: A multiphase formulation for fire propagation in heterogeneous combustible media. *Int. J. Heat Mass Transfer*, **41**, 881–897.

Linn, R., 1997: *A transport model for prediction of wildland fire behavior.* PhD thesis, New Mexico State University.

Linn, R., and P. Cunningham, 2005: Numerical simulations of grass fires using a coupled atmosphere-fire model: Basic fire behavior and dependence on wind speed. *J. Geophysical Research, to appear.*

Linn, R., J. Reisner, J. J. Colman, and J. Winterkamp, 2002: Studying wildfire behavior using firetec. *International J. of Wildland Fire*, **11**, 233–246.

McCaffrey, B. J., 1983: Momentum implications for buoyant diffusion flame. *Combustion and Flame*, **52**, 149–167.

McGrattan, K., and G. Forney, 2004: Fire dynamics simulator (version 4) user's guide. Technical report, NIST. NIST Special Publication 1019.

Mell, W., M. A. Jenkins, J. Gould, and P. Cheney, 2005: A physically based approach to modeling grassland fires. *International J. of Wildland Fire*, **under review**.

Morton, B. R., G. I. Taylor, and J. S. Turner, 1956: Turbulent gravitational convection from maintained and instantaneous source. *Proc. Roy. Sco. London*, **A234**, 1–23.

Morvan, D., and J. Dupuy, 2001: Modeling Fire Spread Through a Forest Fuel Bed Using a Multiphase Formulation. *Comb. Flame*, **127**, 1981–1984.

Morvan, D., V. Tauleigne, and J. Dupuy, 2002a: Flame Geometry and Surface to Crown Fire Transition During the Propagation of a Line Fire Through a Mediterranean Shrub. Millpress, Rotterdam, ISBN 90-77017-72-0.

Morvan, D., V. Tauleigne, and J. Dupuy, 2002b: Wind Effects on Wildfire Propagation Through a Mediterranean Shrub. Millpress, Rotterdam, ISBN 90-77017-72-0.

Ogura, Y., and N. A. Phillips, 1962: Scale analysis of deep and shallow convection in the atmosphere. *J. Atmos. Sci.*, **19**, 173–179.

Porterie, B., D. Morvan, J. Loraud, and M. Larini, 2000: Firespread through fuel beds: Modeling of wind-aided fires and induced hydrodynamics. *Phys. Fluids*, **12**(7), 1762–1782.

Potter, B. E., 2005: The role of released moisture in the atmospheric dynamics associated with wildland fires. *International J. of Wildland Fire*, **14**, 77–84.

Rehm, R. G., and H. R. Baum, 1978: The equations of motion for thermally driven, buoyant flows. *Journal of Research of the NBS*, **83**, 297–308.

Rothermel, R. C., 1972: A mathematical model for predicting fire spread in wildland fuels. In *Research paper INT 115, Intermountain Forest and Range Experiment Station Ogden, Utah, USA*.

Saporte, R., 1966: Sur la determination de la hauteur d'un nuage d'apres deux vues photogrammetriques. *J. Rech. Atmos.*, **2**, 27–35.

Smagorinsky, J., 1963: General circulation experiments with the primitive equation i. the basic experiment. *Mon. Wea. Rev.*, **91**, 99–164.

Xin, Y., 2005: Baroclinic effects on fire flow field. In *Proceedings of the fourth joint meeting of the U.S. sections of the combustion institute*, Combustion Institute, Pittsburgh, Pennsylvania.

Yih, C. S., 1951: Free convection due to point source of heat. In *Proc. First U.S. Nat. Cong. App. Mech.*, p 941.

Zhou, X., and J. Pereira, 2000: A multidimensional model for simulating vegetation fire spread using a porous media sub-model. *Fire and Materials*, **24**, 37–43.

Table 1. 10 m AGL plume–averaged temperature excesses and vertical velocities

Experiment	Temperature Excess (^{o}C)	$\overline{w}$ (m s^{-1})
Meteotron Observations	50	3
FDS simulation (soot plume)	23.0	1.4
FDS simulation (W plume)	40.0	2.7
Clarka (W plume)	4.7	0.82
Clarkb (W plume)	19.32	1.4

APPENDIX

DERIVATION OF BUOYANCY EQUATIONS

1   Buoyancy equation in the FDS simulation

The energy conservation and mass conservation equations are respectively

$$\frac{\partial \rho}{\partial t} + \nabla \cdot (\rho \mathbf{v}) = 0, \tag{1}$$

and

$$\rho \frac{Dh}{Dt} = \frac{Dp}{Dt} - \nabla \cdot \mathbf{q}_r + \nabla \cdot k \nabla T + \sum_l \nabla \cdot h_l \rho D_l \nabla Y_l, \tag{2}$$

where

$$\frac{D}{Dt} = \frac{\partial}{\partial t} + \mathbf{v} \cdot \nabla \mathbf{v}. \tag{3}$$

Here $h = C_p T$ is enthalpy, and C_p is assumed constant. By replacing T with $T - T_e$, Equation 2 is written as

$$\rho \frac{D(C_p(T - T_e))}{Dt} = \frac{Dp}{Dt} - \nabla \cdot \mathbf{q}_r + \nabla \cdot k \nabla T + \sum_l \nabla \cdot h_l \rho D_l \nabla Y_l. \tag{4}$$

Equations 4 and 1 are combined to obtain

$$\frac{\partial(\rho C_p(T - T_e))}{\partial t} + \nabla \cdot \rho C_p(T - T_e)\mathbf{v} = \frac{Dp}{Dt} - \nabla \cdot \mathbf{q}_r + \nabla \cdot k\nabla T + \sum_l \nabla \cdot h_l \rho D_l \nabla Y_l, \quad (5)$$

the flux form of the energy conservation equation. Acceleration due to buoyancy is defined as $B = g\frac{T - T_e}{T_e}$ and when substituted into Equation 5 gives

$$\frac{\partial(\frac{C_p T_e}{g}\rho B)}{\partial t} + \nabla \cdot \frac{C_p T_e}{g}\rho B\mathbf{v} = \frac{Dp}{Dt} - \nabla \cdot \mathbf{q}_r + \nabla \cdot k\nabla T + \sum_l \nabla \cdot h_l \rho D_l \nabla Y_l. \quad (6)$$

With the use of Equation 1, Equation 6 is written as

$$\frac{\partial B}{\partial t} + \nabla \cdot B\mathbf{v} = \frac{g}{C_p \rho T_e}(-\nabla \cdot \mathbf{q}_r + \nabla \cdot k\nabla T + \sum_l \nabla \cdot h_l \rho D_l \nabla Y_l). \quad (7)$$

Equation 7 is the buoyancy equation for the FDS simulations. By defining the buoyancy flux due to the sub-grid scale (SGS) motion, radiation and combustion process as

$$\mathbf{F} = \frac{g}{C_p \rho T_e}(\mathbf{q}_r - k\nabla T - \sum_l h_l \rho D_l \nabla Y_l), \quad (8)$$

and substituting into Equation 7, and integrating over the volume V of the layer, the Equation 7 is written

$$\int_V \frac{\partial B}{\partial t} \, dV + \int_V \nabla \cdot B\mathbf{v} \, dV = \int_V -\nabla \cdot \mathbf{F} \, dV. \quad (9)$$

Applying the divergence theorem to the second term on the left and the term on the right side of Equation 9 gives

$$\int_V \frac{\partial B}{\partial t} \, dV + \int_{\partial V} B\mathbf{v}_h \cdot \hat{\mathbf{n}} \, dS + \int_{bottom}^{top} Bw \, dS = \int_{\partial V} -\mathbf{F} \cdot \hat{\mathbf{n}} \, dS, \quad (10)$$

where $\mathbf{v} = \mathbf{v}_h + w\mathbf{k}$, and $\mathbf{v}_h$ is the horizontal wind. The respective terms on the left side of Equation 10 are buoyancy storage in the layer, buoyancy change due to horizontal advection, and buoyancy change due to vertical convection. The term on the right side of Equation 10 is the buoyancy change due to the SGS motion, radiation and combustion. For boundary conditions $F = 0$ at the top of the simulation domain, Equation 10 is used to calculate the buoyancy flux $\mathbf{F}$ due to the SGS motion, radiation and combustion process at different height levels. Total vertical buoyancy flux is the sum of the vertical convective buoyancy flux and the buoyancy flux due to the SGS motion, radiation and the combustion.

2 Buoyancy equation in the Clark model simulations

The energy conservation and mass conservation equations are respectively

$$\overline{\rho}\frac{\partial \theta}{\partial t} + \overline{\rho}\mathbf{v}, \cdot \nabla \theta = \nabla \cdot (\overline{\rho}K_H \nabla \theta) \tag{11}$$

and

$$\nabla \cdot (\overline{\rho}\mathbf{v}) = 0, \tag{12}$$

where $\overline{\rho}$ is the average density at a certain height level in the Clark model domain, K_H the eddy mixing coefficient for heat and moisture, θ is the potential temperature, and $\mathbf{v}$ is the wind vector. Equations 11 and 12 are combined to form

$$C_p\overline{\rho}\frac{\partial \theta}{\partial t} + \nabla \cdot (C_p\overline{\rho}\mathbf{v}\theta) = \nabla \cdot (C_p\overline{\rho}K_H \nabla \theta), \tag{13}$$

the flux form of the energy conservation equation, where C_p is assumed constant. Integrating Equation 13 over the volume V of a model layer and applying the divergence theorem gives

$$\int_V C_p\overline{\rho}\frac{\partial\theta}{\partial t}\,dV + \int_{\partial V} C_p\overline{\rho}\theta\mathbf{v}\cdot\widehat{\mathbf{n}}\,dS = \int_V \nabla\cdot(C_p\overline{\rho}K_H\nabla\theta)\,dV. \qquad (14)$$

If it is assumed that the environmental temperature field is not disturbed by the convection, then $\partial\theta_e/\partial t = 0$. Substituting $\theta = (\theta - \theta_e) - \theta_e$, $B = g(\theta - \theta_e)/\theta_e$ and $\mathbf{v} = \mathbf{v}_h + w\,\widehat{\mathbf{k}}$ into Equation 14 gives.

$$\int_V \frac{C_p\overline{\rho}\theta_e}{g}\frac{\partial B}{\partial t}\,dV + \int_{\partial V}\frac{C_p\overline{\rho}\theta_e}{g}B\mathbf{v}_h\cdot\widehat{\mathbf{n}}\,dS + \int_{bottom}^{top}\frac{C_p\overline{\rho}\theta_e}{g}Bw\,dS =$$
$$\int_V \nabla\cdot(C_p\overline{\rho}K_H\nabla\theta)\,dV - \int_{\partial V}C_p\overline{\rho}\theta_e\mathbf{v}\cdot\widehat{\mathbf{n}}\,dS. \qquad (15)$$

By integrating over a layer of the domain, and for constant θ_e and $\overline{\rho}$ in the layer, Equation 15 can be written

$$\int_V \frac{\partial B}{\partial t}\,dV + \int_{\partial V}B\mathbf{v}_h\cdot\widehat{\mathbf{n}}\,dS + \frac{g}{C_p\overline{\rho}\theta_e}\int_{bottom}^{top}\frac{C_p\overline{\rho}\theta_e}{g}Bw\,dS =$$
$$\frac{g}{C_p\overline{\rho}\theta_e}\int_V \nabla\cdot(C_p\overline{\rho}K_H\nabla\theta)\,dV - \frac{g}{C_p\overline{\rho}\theta_e}\int_{\partial V}C_p\overline{\rho}\theta_e\mathbf{v}\cdot\widehat{\mathbf{n}}\,dS \qquad (16)$$

The respective terms on the left side of Equation 16 are buoyancy storage in the layer, buoyancy change due to horizontal advection, and buoyancy change due to vertical convection. The respective terms on the right side of Equation 16 are the buoyancy change due to the SGS heat flux and the buoyancy change due to environmental heat flux. In *Clarka* and *Clarkb* simulations θ_e is constant with height, and consequently the contribution of environmental heat flux to the total vertical buoyancy flux is zero. The total vertical buoyancy flux is therefore the sum of the vertical convective buoyancy flux, SGS heat flux, and environmental heat flux.

3 Nomenclature

|	
A	horizontal grid area
B	acceleration due to buoyancy
B	$= g(T - T_e)/T_e$ in FDS
B	$= g(\theta - \theta_e)/\theta_e$ in Clark model
c	Yih (1951)'s constant
C_p	specific heat at constant pressure
D_l	diffusion coefficient of gaseous species l
$\mathbf{F}$	buoyancy flux due to sub-grid scale processes, radiation, and combustion
F_M	plume mass flux based on classical plume theory
F_B	convective buoyancy flux based on classical plume theory
$F_{B(grid)}$	convective buoyancy flux based on model grid data
F	buoyancy flux due to sub-grid scale processes, radiation, and combustion
g	acceleration due to gravity
h	enthalpy of gas
h_l	enthalpy of gaseous species l
k	thermal conductivity
$\widehat{\mathbf{k}}$	unit vertical vector
K_H	eddy mixing coefficient for heat and moisture
$\widehat{\mathbf{n}}$	unit normal vector
p	pressure
p_0	100 kPa pressure
$\mathbf{q}_r$	radiation heat flux vector
R_d	gas constant for dry air
R	effective plume radius
S	model level surface
t	time
T	absolute temperature
T_e	environmental T
$\mathbf{v}$	total wind velocity vector
$\mathbf{v}_h$	horizontal wind vector
V	model layer volume
w	vertical wind velocity component
$\overline{w}$	plume–averaged vertical wind velocity
Y_l	mass fraction of gaseous species l
ρ	total density of gas
$\overline{\rho}$	average density of gas over a model layer in simulation domain
θ	$= T(\frac{p_0}{p})^{R_d/C_p}$ potential temperature
θ_e	environmental potential temperature
∇	total gradient vector
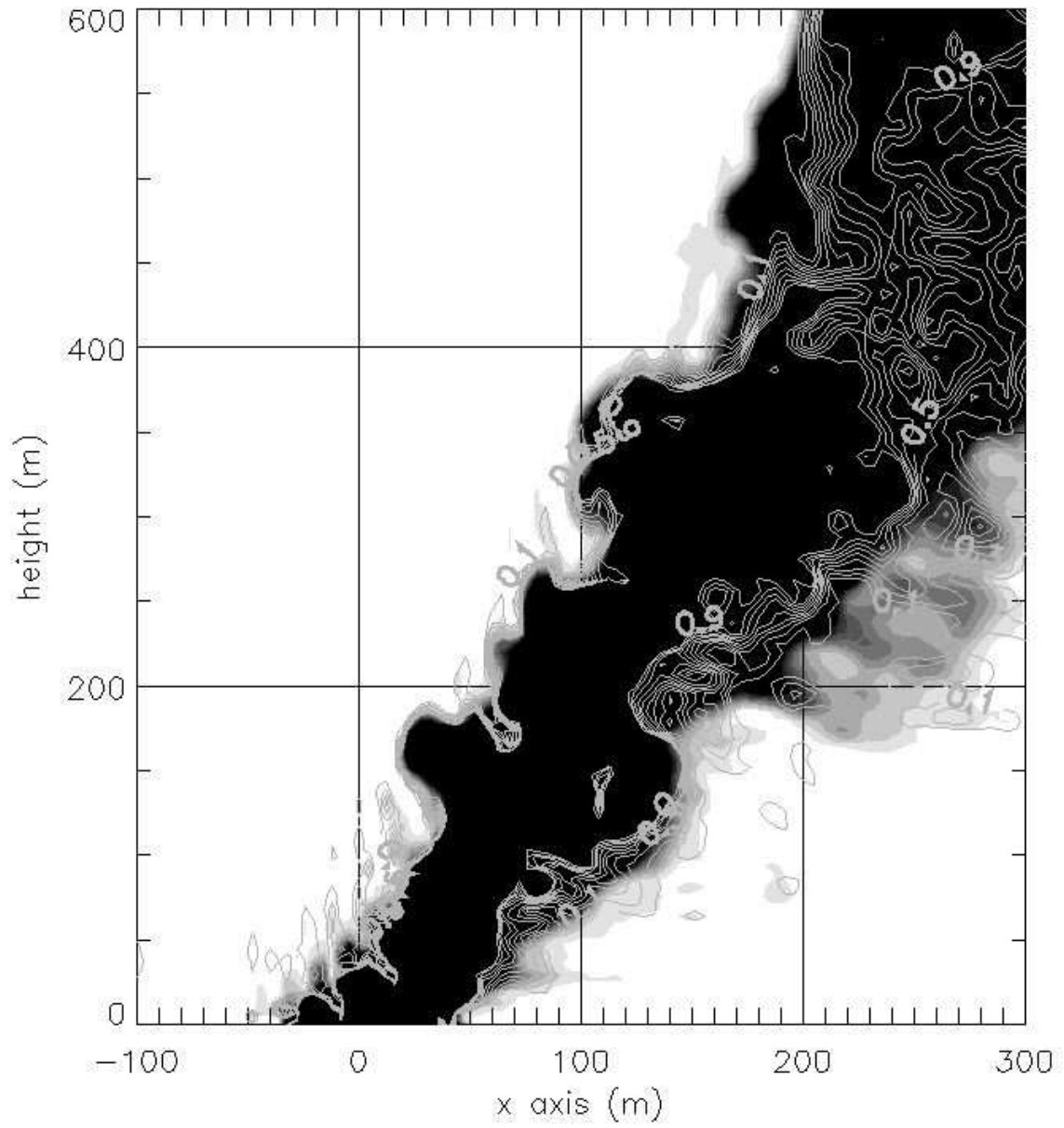
Figure 1. The x-z cross section of FDS smoke photo and soot density contours along the domain centerline.
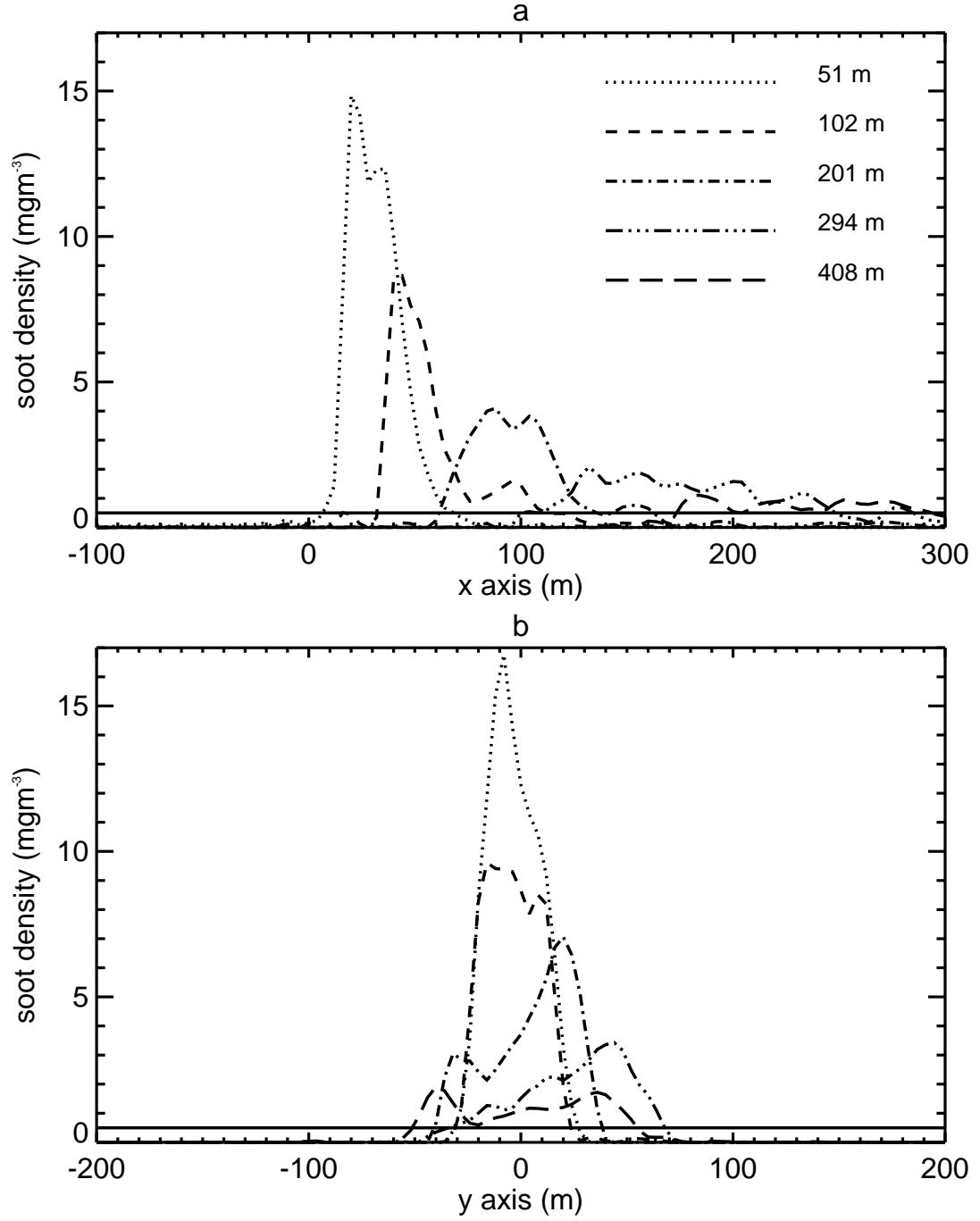
Figure 2. FDS radial profiles at different height levels and 600 s into the simulation of (a) soot density along the domain centerline in x direction and (b) through the point of maximum soot density in the y direction. Horizontal line denotes the soot density of 0.5 mg m^{-3} selected to delineate the plume edge.
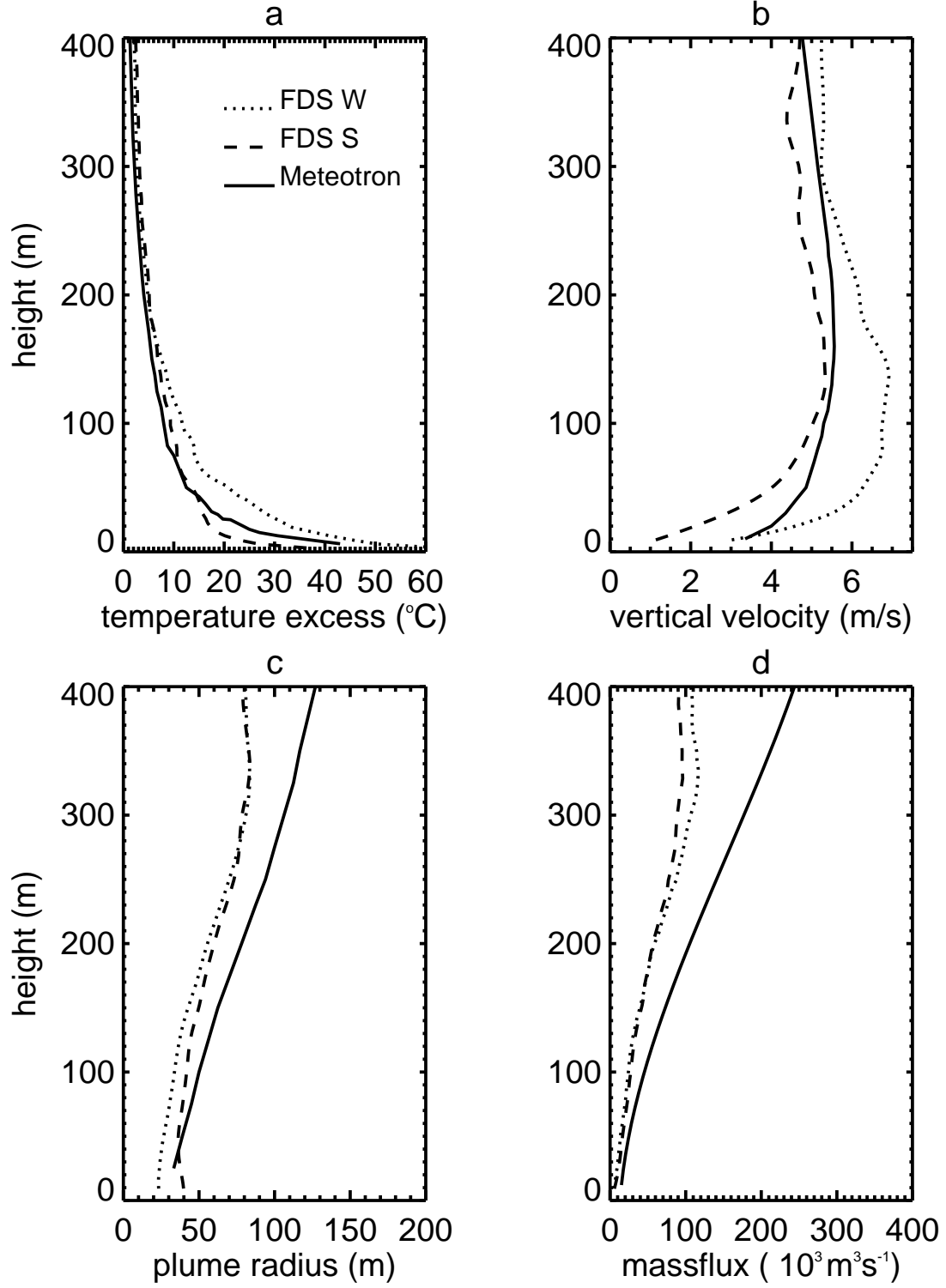
Figure 3. Vertical profiles of plume–averaged properties in the Meteotron experiment (solid line), and FDS simulation determined by W (dotted line) and soot (dashed line) criteria.

Figure 4. Soot density contours on a x-y cross-section of the plume at (a) 103 m AGL and (b) 201 m AGL at 680 s in FDS simulation.
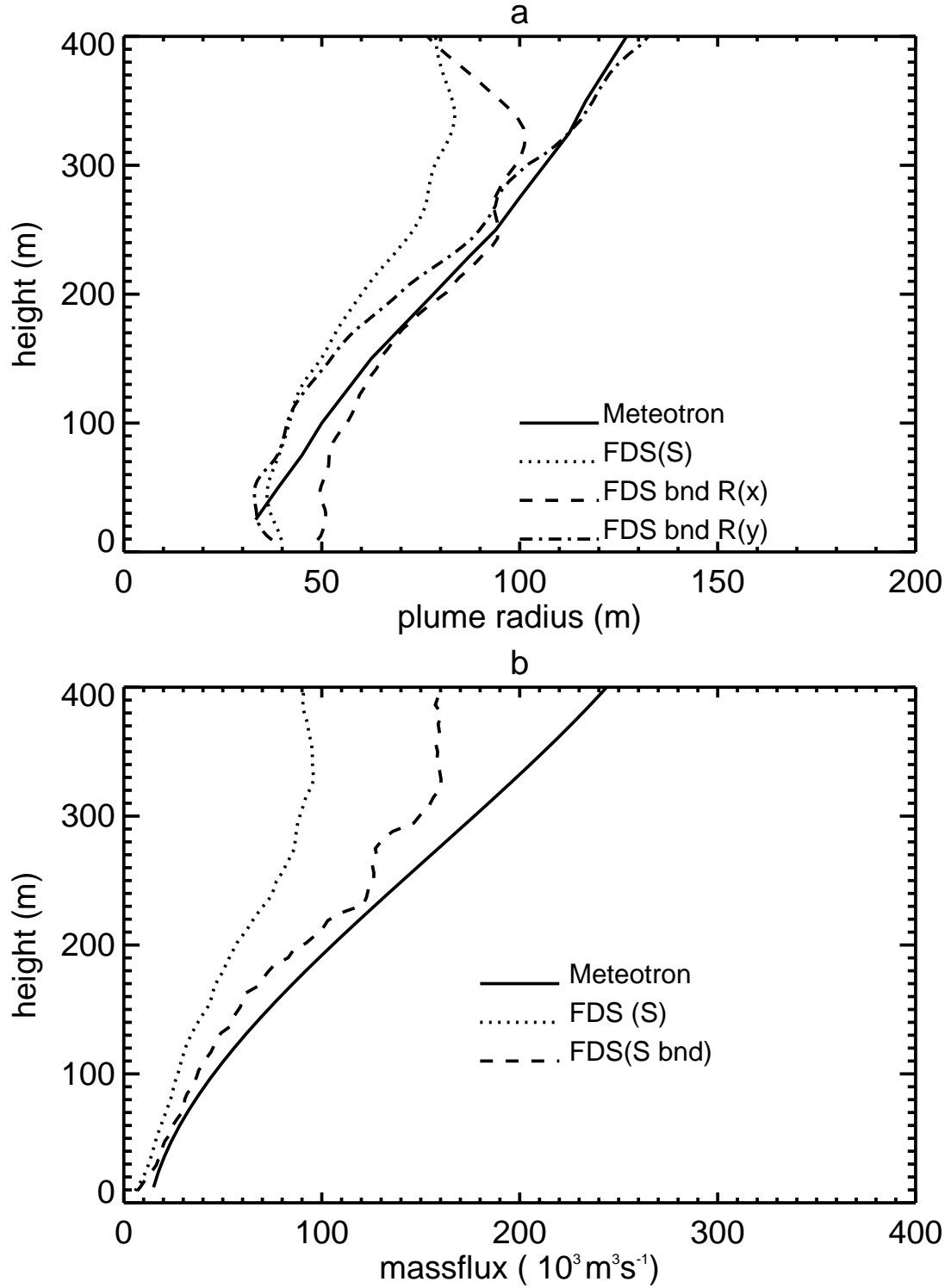
Figure 5. Vertical profiles of (a) Meteotron R (solid line), FDS soot–plume R (dotted line), FDS $R(x)$ plume radius (dashed line), and FDS $R(y)$ plume radius (dashed–dotted line). Vertical profiles of (b) Meteotron mass flux (solid line), FDS soot–plume mass flux based on R (dotted line), and FDS soot–plume mass flux based on $R(x)$ and $R(y)$ radii (dashed line).
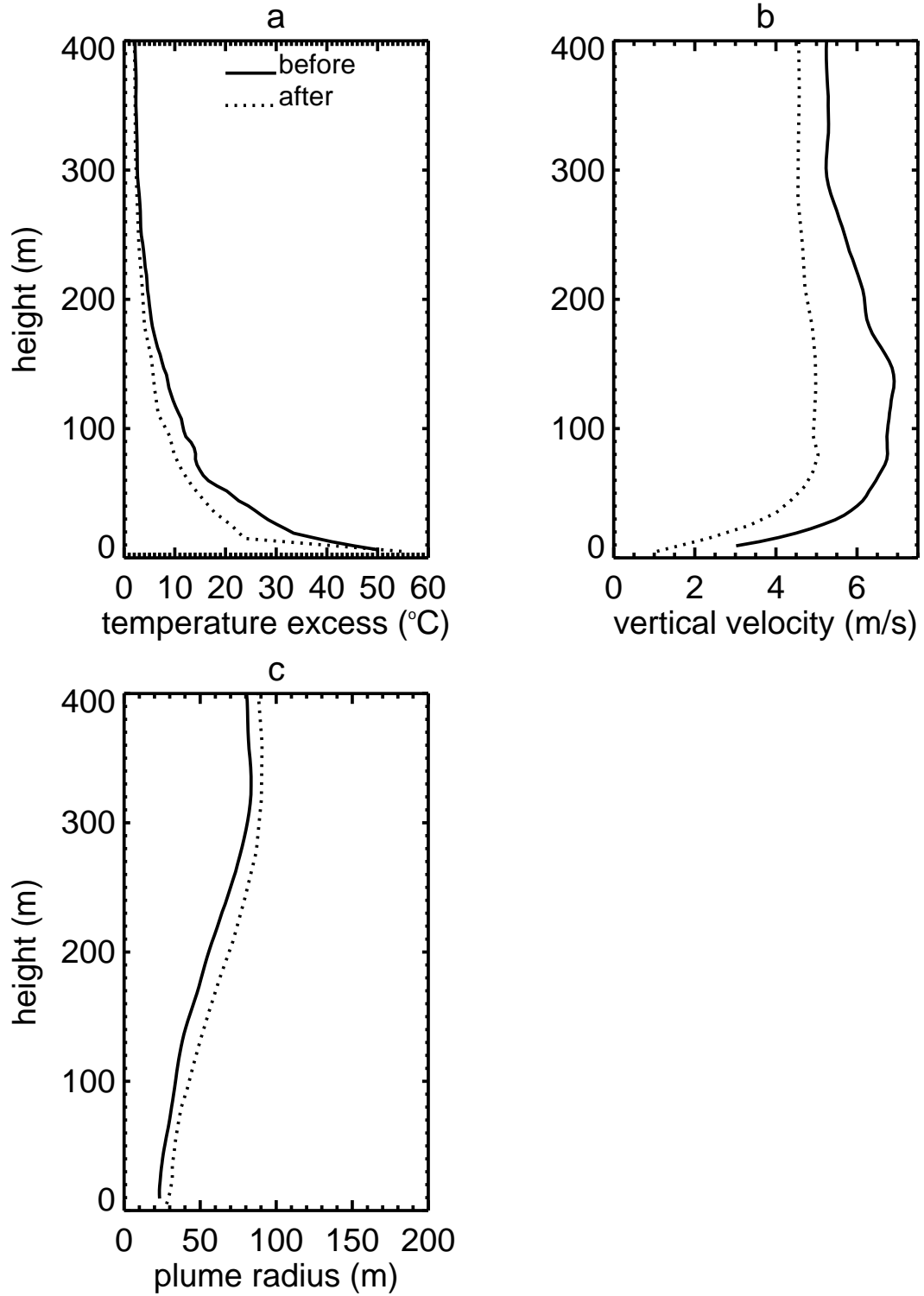
Figure 6. Vertical profiles of W–plume averaged properties in the FDS simulation before (solid line) and after (dotted line) averaging for comparisons between the Clark coupled model simulations and the FDS simulation.
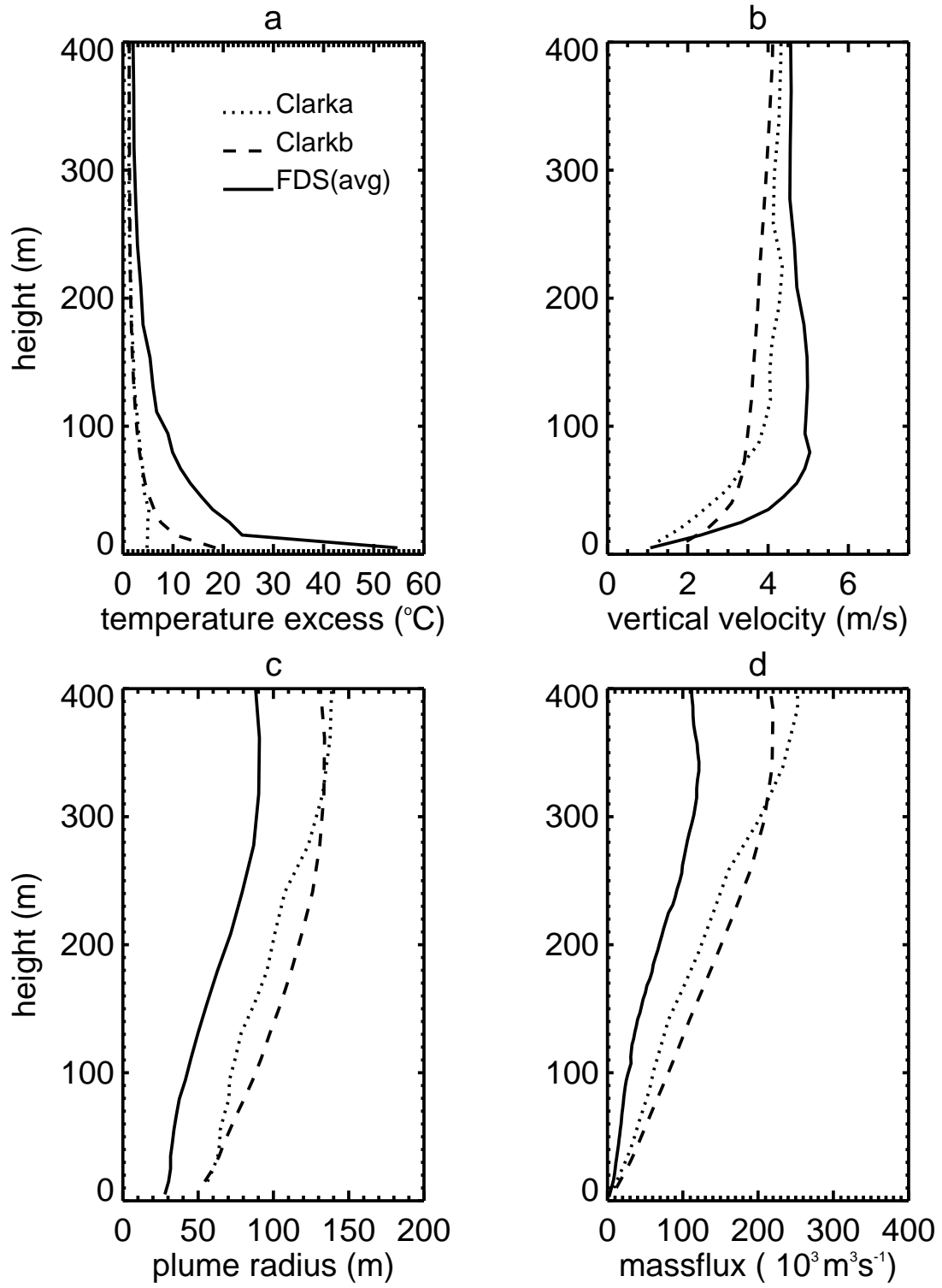
Figure 7. Vertical profiles of the FDS (solid line), *Clarka* (dotted line), and *Clarkb* (dashed line) *W*–plume averaged temperature excess, vertical velocity, plume radius, and plume mass flux.
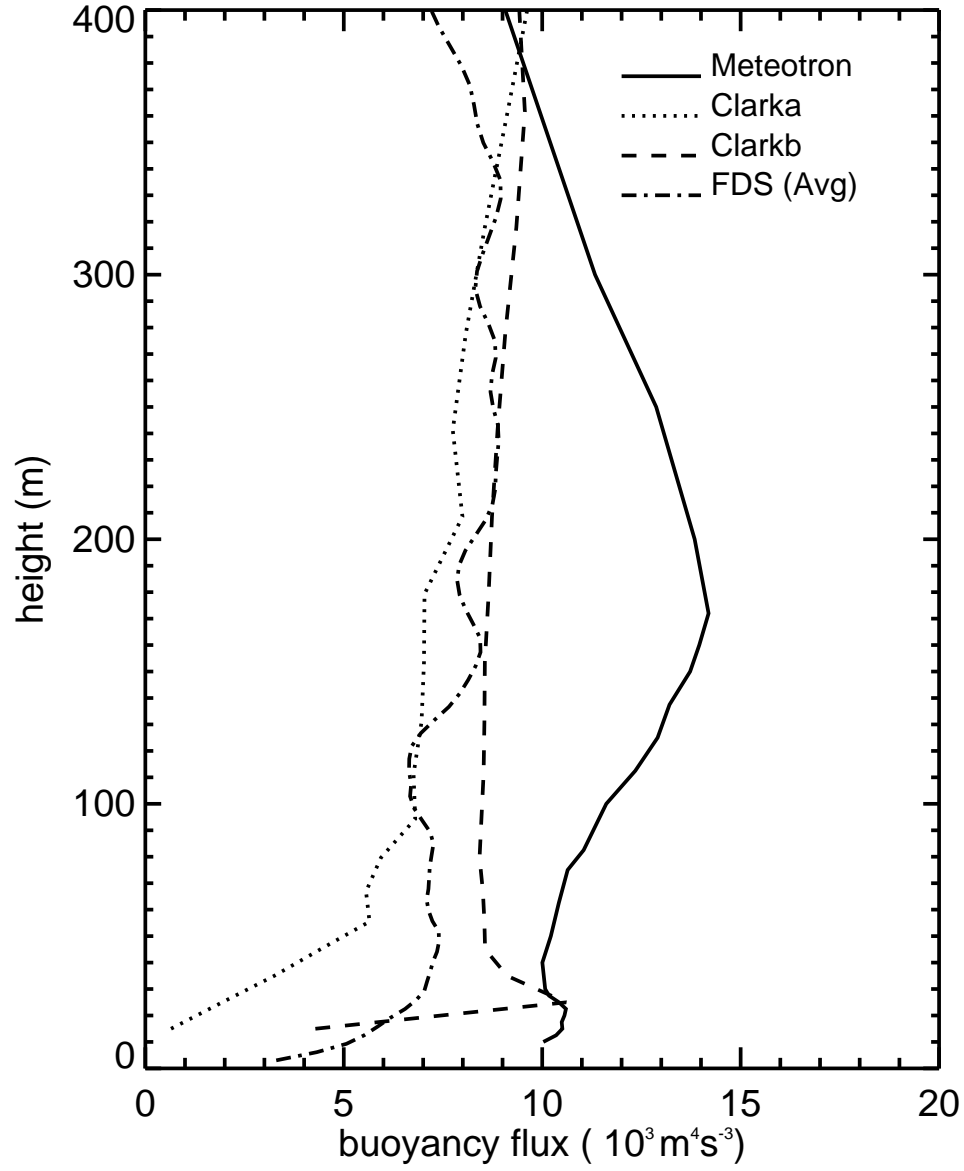
Figure 8. Vertical profiles of the Meteotron experiment (solid line), *Clarka* (dotted line), *Clarkb* (dashed line), and FDS (dotted–dashed line) *W*–plume averaged convective buoyancy fluxes based on Equation 3.
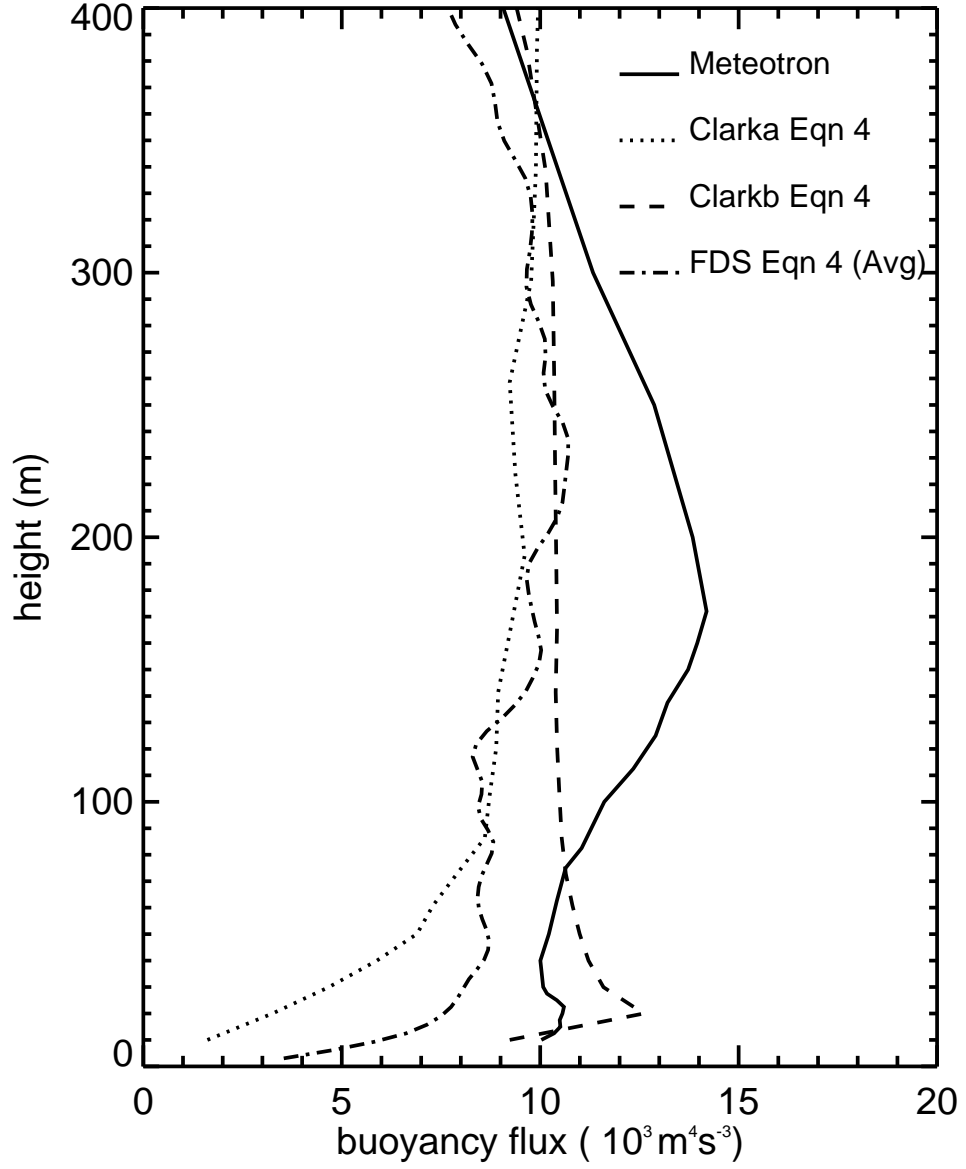
Figure 9. Vertical profiles of the Meteotron experiment (solid line), *Clarka* (dotted line), *Clarkb* (dashed line), and FDS (dotted–dashed line) *W*–plume averaged convective buoyancy fluxes based on Equation 4.
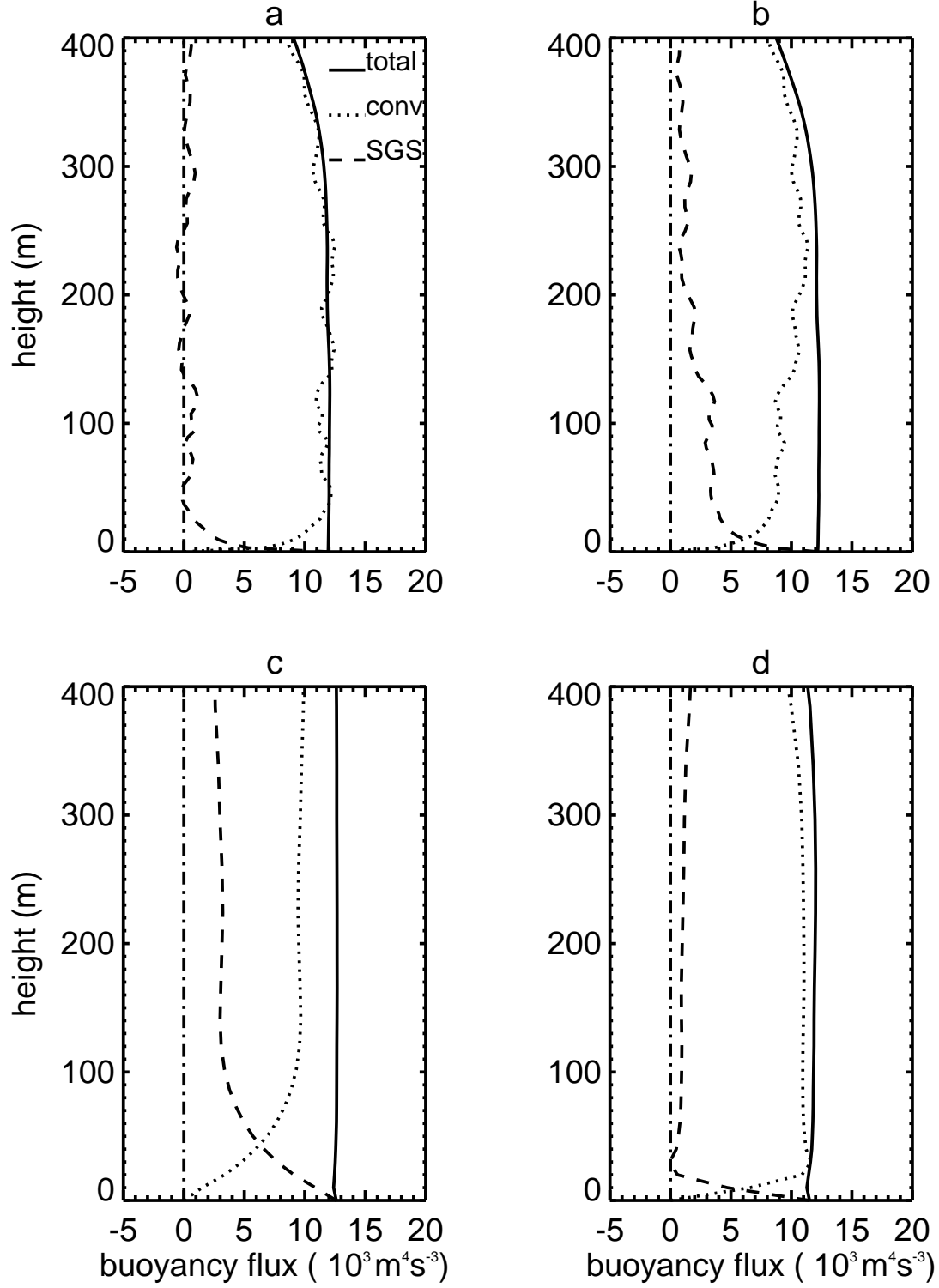
43

Figure 10. Vertical profiles of the total buoyancy flux (solid line), convective buoyancy flux (dotted line), and flux by SGS motion, radiation and combustion (dashed line) in the FDS simulation (a) before and (b) after grid–area averaging and in (c) *Clarka* and (d) *Clarkb*.   44